Achieving Centimeter Accuracy Indoor Localization on Multi-Antenna WiFi Platforms

Chen Chen, *Student Member, IEEE,* Yan Chen, *Senior Member, IEEE,* Yi Han, *Student Member, IEEE,*
Hung-Quoc Lai, *Member, IEEE,* Feng Zhang, *Student Member, IEEE,* and K. J. Ray Liu, *Fellow, IEEE*

***Abstract*—Channel frequency response (CFR) is a fine-grained location-specific information in WiFi systems that can be utilized in indoor positioning systems (IPSs). However, CFR-based IPSs can hardly achieve an accuracy in the centimeter level due to the limited bandwidth in WiFi systems. To achieve such accuracy using WiFi devices, we propose an IPS that fully harnesses the spatial diversity in Multiple-Input-Multiple-Output (MIMO) WiFi systems, which leads to a much larger effective bandwidth. The proposed IPS obtains CFRs associated with locations-of-interest on multiple antenna links during the training phase. Then, in the positioning phase, the IPS captures instantaneous CFRs from an unknown location and computes the resonating strength between the instantaneous CFRs and those obtained in the training phase. The IPS compensates the residual synchronization errors in the calculation of resonating strengths. Extensive experimental results in a typical office environment demonstrate that the proposed IPS achieves true positive rates of 99.93% and 100%, and only incurs false positive rates of 1.56% and 1.80% under the line-of-sight (LOS) and non-line-of-sight (NLOS) scenarios, respectively, with a single pair of WiFi devices. Moreover, results with $0.5cm$ measurement resolution show an accuracy of $1 \sim 2cm$ achieved by the proposed IPS in the NLOS scenario. To the best of our knowledge, this is the first work that can achieve $1 \sim 2cm$ accuracy for NLOS indoor localization using WiFi.**

***Index Terms*—Multiple-input-multiple-output, channel frequency response, time-reversal, resonating strength, indoor localization.**

I. INTRODUCTION

Indoor positioning systems (IPSs) are becoming more and more popular which spawn numerous location-based services (LBS), including campus-wide localization [1], targeted advertisement in supermarkets [2], and shopping mall navigations [3]. The IPSs often demand an accuracy in the sub-meter level, which cannot be achieved by the Global Positioning System (GPS) due to the severe attenuation of GPS signals indoor.

The imperative demands on the high localization accuracy give rise to an extensive development of IPSs leveraging a variety of radio-frequency (RF) techniques [4]. These approaches can be further classified into (i) ranging (ii) fingerprinting. For the ranging-based approaches, the received signal strength (RSS) is commonly used which provides a rough estimation of distances with the free-space path-loss model. SpotON [5] uses the RFID technique to calculate the inter-tag distances based on the RSS readings associated with the received tag, while LANDMARC deploys extra fixed reference tags for calibration to improve the RFID localization precision [6]. Nevertheless, they are only effective in the strong line-of-sight (LOS) scenarios and degrade significantly under the non-line-of-sight (NLOS) scenarios, which is the general case in indoor spaces.

In comparison with the ranging-based schemes, the fingerprinting-based methods can provide better accuracy by collecting spatial features at different locations. Many works exploit the channel impulse response (CIR) in the time domain as location-specific fingerprints. In [7], Patwari *et al.* present the temporal link signature composed by the CIR amplitudes obtained at a direct-sequence spread spectrum (DSSS) receiver to detect the position change of devices. Zhang *et al.* enhance the temporal link signature by incorporating the phase information and compensating the random phase shift [8]. Nevertheless, these approaches require specialized devices, which limits their applicability.

More recently, fingerprinting using WiFi devices has attracted much attention from the academia and the industry since they are built upon the ubiquitous indoor infrastructures of wireless local area networks (WLANs). The RSS is commonly used as the location fingerprint due to its readily availability on WiFi devices. Nevertheless, similar to the RSS-based ranging approaches, the RSS-based fingerprinting schemes suffer from performance loss under the NLOS environments. Meanwhile, RSS only depicts the indoor environment with very limited granularity since it only measures the channel power within a certain frequency band. Thus, RSS-based fingerprinting approaches, including Horus [9], RADAR [10], MultiLoc [11], can only achieve an average accuracy of $2 \sim 5m$.

Channel frequency response (CFR) is another information that can be employed as the spatial feature. CFR is a complex vector characterizing the gains and phases of the subcarriers in orthogonal frequency-division multiplexing (OFDM) systems. Thus, CFR depicts the indoor environment with a much higher granularity than RSS. In [12], Sen *et al.* propose PinLoc that extracts statistics of different locations for localization. With CFRs measured on a 20 MHz frequency band, PinLoc achieves 90% in true positive rate and below 7% in false positive rate across 50 $1m \times 1m$ spots with multiple access points (APs). Utilizing the spatial diversity in multiple-input-multiple-output

---

All the authors are with Origin Wireless, Inc., Greenbelt, MD 20770 USA. Chen Chen, Yi Han, Feng Zhang, and K. J. Ray Liu are also with the Department of Electrical and Engineering, University of Maryland College Park, College Park, MD 20742 USA (e-mail: {cc8834, yhan1990, fzheng15, kjrliu}@umd.edu). Yan Chen is also with University of Electronic Science and Technology of China, Chengdu, Sichuan, China (e-mail: eecyan@uestc.edu.cn). Hung-Quoc Lai is with Origin Wireless Inc. (e-mail: quoc.lai@originwireless.net).

(MIMO) WiFi systems can further boost the localization performances. The Fine-grained indoor fingerprinting system (FIFS) proposed in [13] formulates the compressed fingerprints by aggregating CFR amplitudes of different antenna links, and achieves an accuracy of $1.1m$ under 2×2 MIMO configuration. The accuracy of FIFS is improved to $0.95m$ in [14] by incorporating the phase information contained in the CFRs.

Summarizing the aforementioned schemes based on CIRs or CFRs, we find that the location-specific fingerprints are only of 20 MHz or 40 MHz bandwidth, which introduces ambiguities among different locations. Hence, these schemes can hardly achieve an accuracy in the centimeter level.

Recently, a time-reversal indoor positioning system (TRIPS) is presented in [15] that achieves the centimeter-level accuracy under NLOS scenarios. TRIPS is a single-antenna system that leverages the unique spatial-temporal focusing effect of the time-reversal (TR) technique [16]. With a bandwidth of 125 MHz on 5.4 GHz frequency band, TRIPS achieves an impressive $1 \sim 2cm$ localization accuracy. However, TRIPS requires a dedicated hardware platform and a large bandwidth to resolve enough multipath components in an indoor environment.

Is it possible to achieve the centimeter-level accuracy on a WiFi platform by leveraging the TR technique? The answer is affirmative. In [17], Chen *et al.* utilizes the frequency diversity of WiFi systems by sweeping a large bandwidth composed by multiple WiFi channels and formulates location fingerprints by concatenating the CFRs associated with these channels. One drawback of this approach is that it is time consuming to scan a large number of WiFi channels.

In this paper, we propose an IPS that leverages the spatial diversity inherent in MIMO-OFDM systems to achieve the centimeter-level accuracy. The proposed IPS optimally concatenates the available bandwidths of different antenna links to formulate a much larger effective bandwidth. The IPS consists of two phases: the training phase and the positioning phase. During the training phase, the IPS captures CFRs from multiple locations-of-interest and then combines CFRs of different links into location fingerprints. In the positioning phase, the IPS obtains instantaneous CFRs and evaluates the TR focusing effect by calculating the resonating strengths between the instantaneous CFRs and those acquired in the training phase. Realizing that the inevitable residual synchronization errors in WiFi systems, we develop an algorithm to mitigate the impact of such errors in the computations of the resonating strengths. Finally, the IPS determines the locations according to the resonating strengths.

The main contributions of this work can be summarized as follows:

- We introduce the concept of effective bandwidth as a metric of exploitable diversity for localization.
- We propose an algorithm to fully harness the spatial diversity inherent in MIMO-OFDM WiFi systems to realize the TR focusing effect.
- We conduct extensive experiments in an office environment using a pair of WiFi devices to show that the proposed IPS achieves true positive rates of 99.93% and 100%, while triggering false positive rates of merely 1.56% and 1.80% under LOS and NLOS scenarios respectively with $5cm$-resolution measurement. Moreover, experimental results on a testbed with $0.5cm$ resolution demonstrate that a $1 \sim 2cm$ localization accuracy can be obtained by the proposed IPS. To the best of our knowledge, this is the first work that achieves $1 \sim 2cm$ accuracy for NLOS indoor localization using only a single pair of WiFi devices.

The rest of the paper is organized as follows. In Section II, we introduce the TR technique and the channel estimation in MIMO-OFDM WiFi systems. In Section III, we present the localization algorithm of the proposed IPS. The experimental results are demonstrated and analyzed in Section IV. Finally, Section V concludes the paper and provides some discussions.

II. PRELIMINARIES

In this section, we briefly introduce the TR technique and the channel estimation schemes in WiFi systems.

A. Time-Reversal

TR is a signal processing technique that mitigates the phase distortion of a signal filtered by a linear time-invariant (LTI) system. It leverages the fact that the phase distortion can be removed at a particular time instance when the LTI system $h(t)$ is combined with its time-reversed and conjugated counterpart $h^*(-t)$. The development of TR can be dated back to the 1950s when Bogert uses TR technique to correct a slow picture transmission system delay distortion [18]. Later, Kormylo *et al.* utilize TR in the design of zero-phase digital filters, as the signal is processed in both causal and reverse causal direction to remove the phase distortion [19].

The physical channel can be regarded as LTI if it is inhomogeneous and invertible. When such conditions hold, TR technique can refocus the energy of signal waves at a particular spatial location and a specific time, known as the spatial-temporal focusing effect. This effect is verified experimentally in the field of ultrasonics, acoustics, and electromagnetism [16], [20], [21], [22]. More recently, TR is applied to the broadband wireless communication systems [23].

The concept of TR communication is illustrated in Fig. 1. When transceiver A intends to send information to transceiver B, transceiver B sends a probing signal to transceiver A, which is termed as the *channel probing phase*. Upon reception of the probing signal, transceiver A extracts the CIR, time-reverses, and takes conjugate to generate a signature. In the second phase, termed as the *TR transmission phase*, transceiver A convolves the transmitted symbols with the signature and sends to transceiver B. The channel acts as a matched filter during the transmission due to the time-reversal operation. The TR focusing peak can be observed at a specific time instance at transceiver B, the source location of the channel probing phase. It is by virtue of the TR focusing effect at the intended location that TR technique is employed successfully in indoor positionining applications [15].

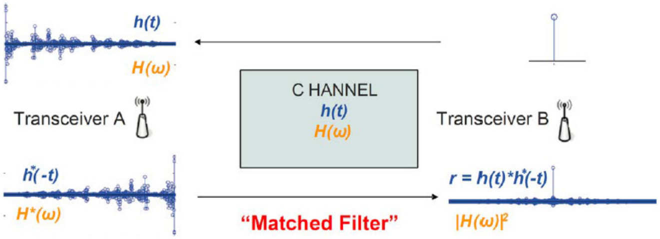

Fig. 1: A simple TR wireless communication system.

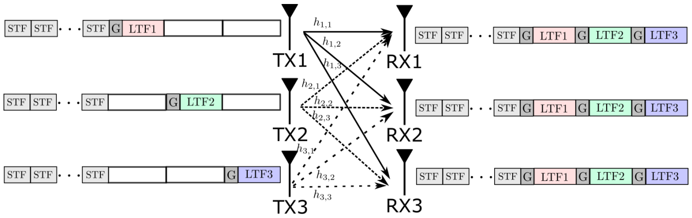

Fig. 2: Channel estimation in MIMO-OFDM WiFi system.

B. *Channel Estimation in MIMO-OFDM*

Assume an MIMO-OFDM system with N_t transmitting antennas and N_r receiving antennas, and denote the CIR between transmitting antenna (TX) n_t and receiving antenna (RX) n_r as $h_{n_t,n_r}[\ell]$ where ℓ runs from 0 to $L_{n_t,n_r}-1$, and L_{n_t,n_r} is the number of multipath components between TX n_t and RX n_r. To facilitate timing/frequency synchronization and channel estimation, TX n_t sends a training sequence $x_{n_t}[n]$ composed by several short training fields (STFs), guard intervals (G), and N_t long training fields (LTFs). The n-th sample of the received signal at RX n_r can be expressed as

$$y_{n_r}[n] = \sum_{n_t=1}^{N_t} \sum_{l=0}^{L_{n_t,n_r}-1} h_{n_t,n_r}[l] x_{n_t}[n-l] + w_{n_r}[n] \ , \quad (1)$$

where $w_{n_r}[n]$ is the channel noise at RX n_r. With the help of STFs, RX n_r detects the starting position of the first LTF. Then, it performs N-point fast Fourier transform (FFT) on all LTFs. After discarding the null subcarriers, the frequency domain representation of $y_{n_r}[n]$ on the k-th usable subcarrier associated with the i-th LTF takes the form

$$Y_{i,n_r}[u_k] = \sum_{n_t=1}^{N_t} H_{n_t,n_r}[u_k] X_{i,n_t}[u_k] + W_{i,n_r}[u_k] \ , \quad (2)$$

where u_k is the index for the k-th subcarrier, and $k = 1, 2, \cdots, N_u$. Here, N_u is the number of usable subcarriers, $H_{n_t,n_r}[u_k]$ is the frequency domain representation of $\{h_{n_t,n_r}[\ell]\}_{\ell=0,1,\cdots,L_{n_t,n_r}-1}$ on the k-th subcarrier, $X_{i,n_t}[u_k]$ is the frequency domain representation of $x_{n_t}[n]$ with n in the range of the i-th LTF on the k-th subcarrier, and $W_{i,n_t}[u_k]$ is the frequency domain noise of the i-th LTF on the k-th subcarrier.

Fig. 2 illustrates the channel estimation procedure in MIMO-OFDM WiFi systems [24]. The TX transmits LTFs alternatively such that at any given time instance, only one TX is sending the LTF. Thus, $X_{i,n_t}[u_k]$ is expressed by

$$X_{i,n_t}[u_k] = X[u_k] \mathbb{1}(i = n_t) \ , \quad (3)$$

where $\mathbb{1}(x)$ is the indicator function. Substituting $X_{i,n_t}[u_k]$ back into (2) gives

$$Y_{i,n_r}[u_k] = \Big[H_{i,n_r}[u_k] X[u_k] + W_{i,n_r}[u_k] \Big] \mathbb{1}(i = n_t) \ . \quad (4)$$

The CFR $H_{n_t,n_r}[u_k]$ is estimated by

$$\hat{H}_{n_t,n_r}[u_k] = \frac{Y_{n_t,n_r}[u_k]}{X[u_k]} = H_{n_t,n_r}[u_k] + \frac{W_{n_t,n_r}[u_k]}{X[u_k]} \ . \quad (5)$$

Eq. (5) depicts $H_{n_t,n_r}[u_k]$ in the ideal case. In practice, the WiFi receivers suffer from the carrier frequency offset (CFO), sampling frequency offset (SFO), and symbol timing offset (STO) caused by the mismatches of analog and digital components between the transmitters and receivers. Although WiFi receivers perform synchronization, the residual synchronization errors cannot be neglected. Meanwhile, the phase locked loops (PLLs) at the WiFi receivers produce random common phase offsets (CPO), which should be incorporated into CFRs.

In presence of these synchronization errors, the channel estimation at RX n_r takes the form [25]

$$\hat{H}_{n_t,n_r}[u_k] = H_{n_t,n_r}[u_k] e^{j\nu_{n_r}} \times e^{j2\pi\left(\alpha_{n_t}(\Delta s_{n_r}, \Delta\omega_{n_r}) + \epsilon_{n_t}(\Delta\psi_{n_r}, \Delta\eta_{n_r}) u_k\right)} + U_{n_t,n_r}[u_k] \ , \quad (6)$$

where $U_{n_t,n_r}[u_k]$ is the estimation noise between TX n_t and RX n_r, Δs_{n_r} is the reference absolute time of the detected frame starting point after timing synchronization using STFs,

$$\alpha_{n_t}(\Delta s_{n_r}, \Delta\omega_{n_r}) = \frac{\left(\Delta s_{n_r} + (i-1)N_s + N_G + \frac{N}{2}\right)\Delta\omega_{n_r}}{N} \ , \quad (7)$$

$$\epsilon_{n_t}(\Delta\psi_{n_r}, \Delta\eta_{n_r}) = \frac{\Delta\psi_{n_r} + \left((i-1)N_s + N_G + \frac{N}{2}\right)\Delta\eta_{n_r}}{N} \ , \quad (8)$$

are the initial and linear phase distortions respectively, N_G is the length of the guard interval, and $N_s = N_G + N$ is the total length of one OFDM block.

To illustrate the impact of phase distortions on CFRs, we show the normalized amplitudes and phases of 200 CFRs captured within 4 seconds in Fig. 3(a) and Fig. 3(b). Despite the consistency in the normalized amplitudes, the variations in the phases caused by the aforementioned initial and linear phase distortions are severe and thus must be compensated.

III. ALGORITHM DESIGN

A. *Calculating TR Resonating Strength for Each Link*

Given two CIRs $\hat{\mathbf{h}} = \left[\hat{h}[0], \hat{h}[1], \cdots, \hat{h}[L-1]\right]^{\mathsf{T}}$ and $\hat{\mathbf{h}}' = \left[\hat{h}'[0], \hat{h}'[1], \cdots, \hat{h}'[L-1]\right]^{\mathsf{T}}$, where $(\cdot)^{\mathsf{T}}$ represents the

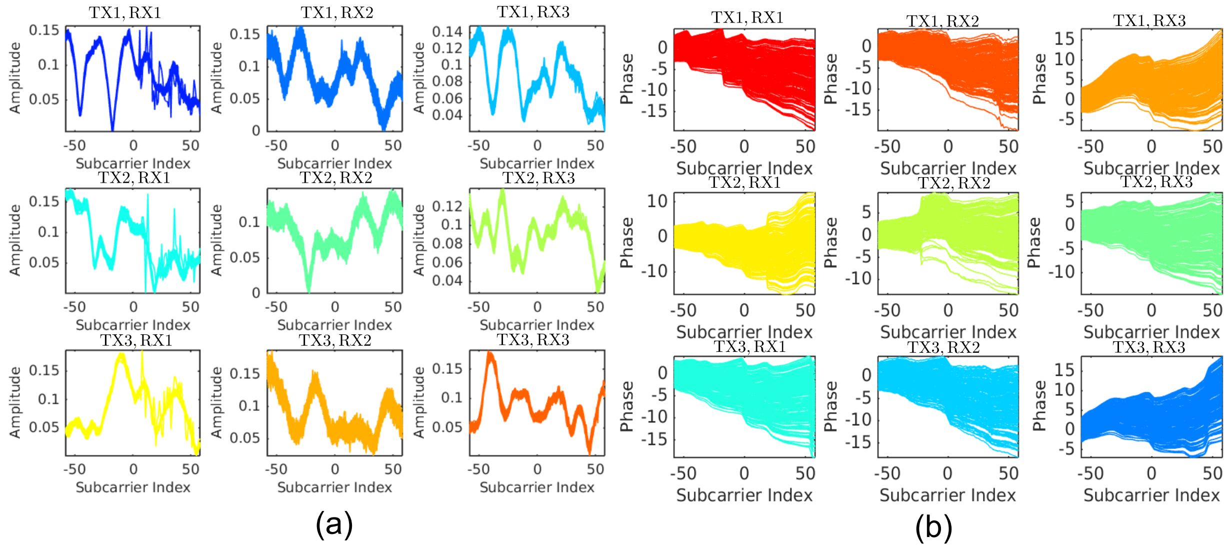

Fig. 3: A snapshot of CFRs of 9 links in a 3×3 MIMO-OFDM system collected in 4 seconds. (a) Normalized amplitudes (b) Unwrapped phases.

transpose operator, the resonating strength between them is given by [15]

$$\gamma_{\mathsf{CIR}}[\hat{\mathbf{h}}, \hat{\mathbf{h}}'] = \left(\frac{\max_i \left| \left(\hat{\mathbf{h}} * \hat{\mathbf{h}}' \right) [i] \right|}{\sqrt{\langle \hat{\mathbf{h}}, \hat{\mathbf{h}} \rangle} \sqrt{\langle \hat{\mathbf{h}}', \hat{\mathbf{h}}' \rangle}} \right)^2, \tag{9}$$

where $*$ stands for the linear convolution, and $\langle \mathbf{x}, \mathbf{y} \rangle$ is the inner product operator between vector $\mathbf{x}$ and $\mathbf{y}$ calculated as $\mathbf{x}^{\dagger}\mathbf{y}$, and $(\cdot)^{\dagger}$ is the Hermitian operator. By taking maximum over all possible i in the calculation of $\gamma_{\mathsf{CIR}}[\hat{\mathbf{h}}, \hat{\mathbf{h}}']$, the impact of STO is mitigated.

Since cross correlation in time domain is equivalent to inner product in frequency domain, we redefine the resonating strength calculated from CFRs in the frequency domain, and extend (9) into MIMO-OFDM systems. Assume two CFRs $\hat{\mathbf{H}}_{n_t,n_r}$ and $\hat{\mathbf{H}}'_{n_t,n_r}$ measured between TX n_t to RX n_r. For convenience, we define the *link index* $d = (n_t - 1)N_r + n_r$[1]. Then, $\hat{\mathbf{H}}_d$ is expressed as

$$\hat{\mathbf{H}}_d = \begin{bmatrix} \hat{H}_d[u_1] & \hat{H}_d[u_2] & \cdots & \hat{H}_d[u_k] & \cdots & \hat{H}_d[u_{N_u}] \end{bmatrix}^{\mathsf{T}}. \tag{10}$$

Similar definitions apply for $\hat{\mathbf{H}}'_d$. Given $\hat{\mathbf{H}}_d$ and $\hat{\mathbf{H}}'_d$, we define the *resonating strength* on link d as

$$\overline{\phi}_d = \frac{\max_{\epsilon} \left| \sum_{k=1}^{N_u} \hat{H}_d[u_k] \hat{H}'_d[u_k] e^{j\epsilon u_k} \right|^2}{\Lambda_d \Lambda'_d}, \tag{11}$$

where

$$\Lambda_d = \langle \mathbf{H}_d, \mathbf{H}_d \rangle, \ \Lambda'_d = \langle \mathbf{H}'_d, \mathbf{H}'_d \rangle \tag{12}$$

are the *link gains* for $\mathbf{H}_d$ and $\mathbf{H}'_d$, respectively.

Calculating $\overline{\phi}_d$ requires an accurate estimation of ϵ. To obtain ϵ efficiently, we employ an FFT with size N_{ser}, leading to a searching resolution of $2\pi/N_{\mathsf{ser}}$ in the range of $[0, 2\pi)$ for $\overline{\phi}_d$. The algorithm is summarized into Algorithm 1.

Algorithm 1 Calculating the resonating strength $\overline{\phi}_d$

```
Input: ${\hat{H}_d[u_k]}_{k=1,2,\cdots,N_u}$, ${\hat{H}'_d[u_k]}_{k=1,2,\cdots,N_u}$
Output: $\overline{\phi}_d$
Intializing $\Lambda_d = 0$ and $\Lambda'_d = 0$
for $k = 1, 2, \cdots, N_u$ do
    Calculating $\hat{G}[u_k] = \hat{H}_d[u_k]\hat{H}'^*_d[u_k]$
    Calculating $\Lambda_d = \Lambda_d + \hat{H}_d[u_k]\hat{H}^*_d[u_k]$
    Calculating $\Lambda'_d = \Lambda'_d + \hat{H}'_d[u_k]\hat{H}'^*_d[u_k]$
end for
Appending $(N_{ser} - N_u)$ zeros at the end of ${\hat{G}[u_k]}_{k=1,2,\cdots,N_u}$ if $N_{ser} \geq N_u$. Otherwise, discarding
    the last $(N_u - N_{ser})$ entries of ${\hat{G}[u_k]}_{k=1,2,\cdots,N_u}$.
Performing an $N_{ser}$-point FFT on ${\hat{G}[u_k]}_{k=1,2,\cdots,N_u}$, which leads to ${g[n]}_{n=1,2,\cdots,N_{ser}}$ given as
    $g[n] = \sum_{k=1}^{N_{ser}} \hat{G}[u_k] e^{-j \frac{2\pi n(k-1)}{N_{ser}}}$.        (13)
Calculating $\overline{\phi}_d = \frac{\max_{n=1,2,\cdots,N_{ser}} |g[n]|^2}{\Lambda_d \Lambda'_d}$.
return $\overline{\phi}_d$
```

As can be seen from by the numerator of (11), the impact of linear phase distortion given in (8) is mitigated by the searching of ϵ. Moreover, the impact of initial phase distortion given in (7) is eliminated by taking the absolute value.

B. Fusing TR Resonating Strength of Different Links

Assuming that we obtain the CFRs from all of the D links, given as

$$\hat{\mathbb{H}} = \begin{bmatrix} \hat{\mathbf{H}}_1^{\mathsf{T}} & \hat{\mathbf{H}}_2^{\mathsf{T}} & \cdots & \hat{\mathbf{H}}_d^{\mathsf{T}} & \cdots & \hat{\mathbf{H}}_D^{\mathsf{T}} \end{bmatrix}^{\mathsf{T}} \tag{14}$$

with $\hat{\mathbb{H}}'$ defined similarly, we calculate $\{\overline{\phi}_d\}_{d=1,2,\cdots,D}$ and fuse them together into the combined resonating strength

---

[1] For instance, in a 3×3 MIMO system, the link between transmitter 2 and receiver 1 is labeled as link 4.

$\gamma[\hat{\mathbb{H}}, \hat{\mathbb{H}}']$, expressed by

$$\gamma[\hat{\mathbb{H}}, \hat{\mathbb{H}}'] = \left(\sum_{d=1}^{D} \omega_d \sqrt{\bar{\phi}_d} \right)^2 , \tag{15}$$

where

$$\omega_d = \frac{\sqrt{\Lambda_d \Lambda'_d}}{\sqrt{\sum_{d=1}^{D} \Lambda_d} \sqrt{\sum_{d=1}^{D} \Lambda'_d}} \tag{16}$$

is the weight for the d-th link. The denominator of ω_d scales $\gamma[\hat{\mathbb{H}}, \hat{\mathbb{H}}']$ into the range of $[0, 1]$.

C. Effective Bandwidth

Since we fully utilize the information contained in $\hat{\mathbb{H}}$ and $\hat{\mathbb{H}}'$ in the computation of the combined resonating strength $\gamma[\hat{\mathbb{H}}, \hat{\mathbb{H}}']$, we achieve an effective bandwidth $\mathbb{W}$ given by

$$\mathbb{W} = \frac{D N_u B}{N} , \tag{17}$$

where B is the bandwidth per link. For 802.11n WiFi systems, B can be as large as 40 MHz.

D. Localization Using Combined Resonating Strength

The localization in the proposed IPS consists of two phases: (i) training phase (ii) positioning phase. We elaborate on the two phases in the subsequent parts of this section.

1) Training Phase: During the training phase, we collect R CFR snapshots from each of the L locations-of-interest. The $L \times R$ CFRs are stored into the training database $\mathbb{D}_{\mathsf{train}}$. The i-th column of $\mathbb{D}_{\mathsf{train}}$ is given by $\hat{\mathbb{H}}_i$, with $\hat{\mathbb{H}}_i$ shown as (14), and i is the *training index*. Denote the snapshot index as r and the location index as ℓ, the training index i can be mapped from (r, ℓ) as $i = (\ell - 1)R + r$.

2) Positioning Phase: In the positioning phase, assume that we collect the instantaneous CFR $\hat{\mathbb{H}}'$ at an unknown location ℓ'. To estimate ℓ', we first calculate the resonating strengths between each CFR in $\mathbb{D}_{\mathsf{train}}$ and $\hat{\mathbb{H}}'$ which leads to $\{\gamma[\hat{\mathbb{H}}_i, \hat{\mathbb{H}}']\}_{i \in \mathcal{L}}$, where $\mathcal{L} = \{0, 1, 2, \cdots, L\}$ is the candidate set of possible locations. The location index 0, termed as the *null location*, is also included into $\mathcal{L}$ since it is possible that the instantaneous CFR is obtained at an unmapped location.

Based on $\{\gamma[\hat{\mathbb{H}}_i, \hat{\mathbb{H}}']\}_{i \in \mathcal{L}}$, we search for the training index i that best matches the instantaneous CFR. The estimated training index $\widehat{i}$ can be written as

$$\widehat{i} = \begin{cases} \underset{i=1,2,\cdots,L}{\operatorname{argmax}} \ \gamma[\hat{\mathbb{H}}_i, \hat{\mathbb{H}}'], & \underset{i=1,2,\cdots,L}{\max} \ \gamma[\hat{\mathbb{H}}_i, \hat{\mathbb{H}}'] \geq \Gamma \\ 0, & \text{Otherwise} , \end{cases} \tag{18}$$

where Γ is the threshold. Finally, the estimated location index $\hat{\ell}'$ is mapped back from $\widehat{i}$ by

$$\hat{\ell}' = \begin{cases} \operatorname{mod}(\widehat{i} - 1, R) + 1, & \widehat{i} \neq 0 \\ 0, & \text{Otherwise} , \end{cases} \tag{19}$$

where $\operatorname{mod}(x, y)$ is the modulus operator on x with base y.

IV. EXPERIMENTAL RESULTS

A. Experiment Settings

1) Environment: The experiments are conducted in a typical office in a multi-storey building. The indoor space is occupied by desks, computers, chairs, and shelves.

2) Devices: We build several prototypes of WiFi platforms using off-the-shelf WiFi devices which support 3×3 MIMO configuration. Based on functionalities of these WiFi platforms in the experiment, they can be further classified as (i) AP (ii) Stations (STAs). One AP can be associated with several STAs simultaneously. Upon request, the AP broadcasts special WiFi packets to all connected STAs. Upon reception of the special packets, each STA estimates the CFR between the AP and itself. The estimated CFRs are then feedbacked from the STAs to the AP. In our experiments, all WiFi devices configure their center frequencies at 5.24 GHz.

3) Details of Experiments: The experiment settings are illustrated in Fig. 4 with details elaborated below:

Exp. 1: We evaluate the localization performance of the proposed algorithm with a $5cm$ resolution. The AP is placed at two different positions in the office to establish both LOS and NLOS links with the STA. For each AP position, we measure CFRs of 100 locations on a testbed with a unit distance of $5cm$. For each location, we record 10 CFRs.

Exp. 2: We study the achievable localization accuracy of the proposed IPS. The STA is placed at the same testbed with Exp. 1, but with a finer resolution of $0.5cm$. We measure CFRs 400 locations on the grid points of a 20×20 rectangular grid on the testbed. For each location, we obtain 5 CFRs.

Exp. 3: We investigate the impact of human activities on the localization performance. One participant is asked to wander randomly in the vicinity of the STA placed on the testbed as in Exp. 1 with $5cm$ unit distance. The distances between the participant and the STA range from 8 to 10 feet. The AP is placed at the same NLOS position as Exp. 1. CFRs from 40 different locations on the testbed are collected, with 10 CFRs per location.

Exp. 4: We study the impact of door opening/closing on the localization performance. The AP is placed in an office room, with STA located in a closet near the entrace of the office. The direct link between the AP and the STA is blocked by two concrete walls. Then, we open/close the door of a room in the middle between the AP and STA. CFRs from 4 STA positions in the closet are captured with 10 CFRs per location.

Exp. 5: We perform a long-term study on the performance of the proposed IPS. One AP and four STAs are deployed in the office. The CFRs are collected every 10 minutes from the four STAs. The IPS is kept running for 97 hours (4 days and 5 hours) without interruption, covering weekends and weekdays. For each measurement, we collect 5 CFRs from each STA.

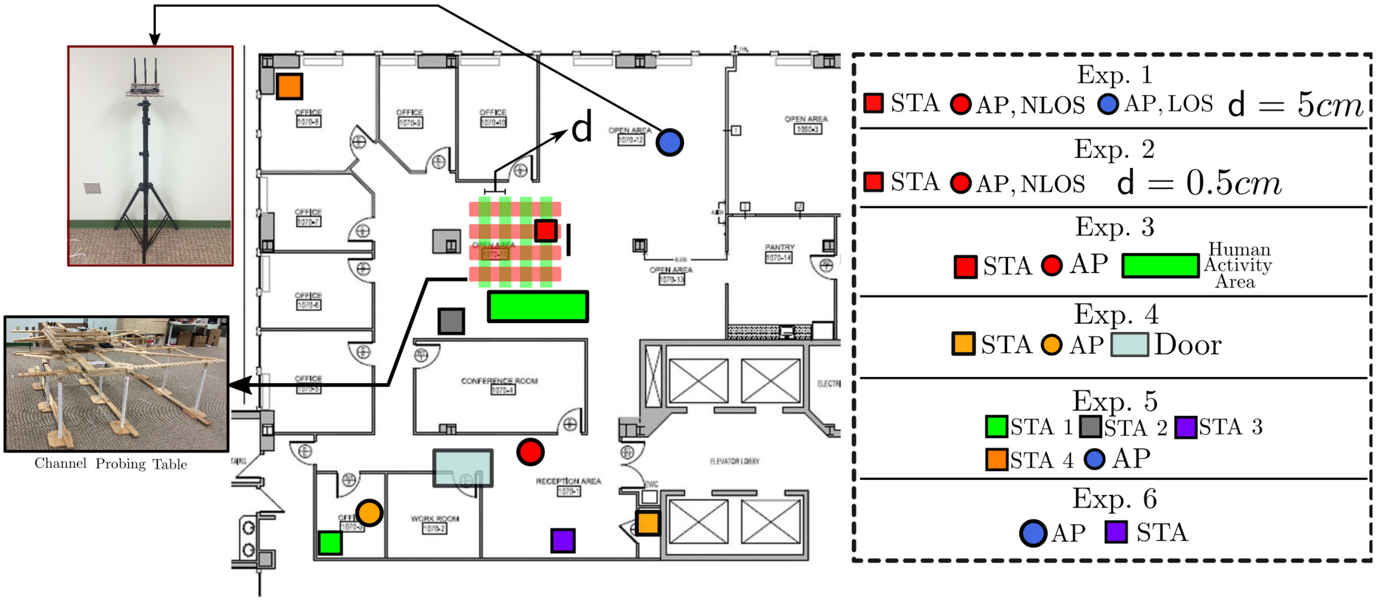

Fig. 4: Setups for the experiments.

	Effective Bandwidth (MHz)	35	71	107	143	178	214	249	285	321
Exp. 1 NLOS	Γ	0.78	0.72	0.63	0.60	0.59	0.56	0.55	0.54	0.54
	$\mathbb{P}_{\mathsf{TP}}(\%)$	100	100	100	100	100	100	100	100	100
	$\mathbb{P}_{\mathsf{FP}}(\%)$	1.73	1.85	1.77	1.82	1.64	1.74	1.56	1.80	1.80
Exp. 1 LOS	Γ	0.86	0.74	0.70	0.71	0.68	0.67	0.65	0.64	0.64
	$\mathbb{P}_{\mathsf{TP}}(\%)$	100.00	99.73	99.84	99.91	99.98	99.84	99.91	99.93	99.93
	$\mathbb{P}_{\mathsf{FP}}(\%)$	1.98	1.98	1.70	1.67	1.69	1.66	1.93	1.56	1.56
Exp. 3 Human Activities	Γ	0.84	0.72	0.65	0.62	0.60	0.56	0.56	0.53	0.53
	$\mathbb{P}_{\mathsf{TP}}(\%)$	97.94	98.61	99.83	99.94	99.61	99.89	99.94	99.89	99.89
	$\mathbb{P}_{\mathsf{FP}}(\%)$	1.72	1.56	1.87	1.97	1.53	1.81	1.64	1.94	1.94
Exp. 4 Door Effect	Γ	-	-	-	-	-	-	0.54	0.53	0.51
	$\mathbb{P}_{\mathsf{TP}}(\%)$	-	-	-	-	-	-	92.00	91.38	98.37
	$\mathbb{P}_{\mathsf{FP}}(\%)$	-	-	-	-	-	-	1.62	1.83	1.70

TABLE I: Settings of Γ to achieve $\mathbb{P}_{\mathsf{TP}} \geq 90\%$ and $\mathbb{P}_{\mathsf{FP}} \leq 2\%$.

Exp. 6**:** We conduct this experiment to analyze the impact of initial phase variations on the performance. We fix the positions of both AP and STA, and plug in and out the power supply of the AP to enforce the reinitialization of the PLL at the AP. After each power cycling, we collect 10 CFRs. The same procedure is repeated 20 times.

The effective bandwidths $\mathbb{W}$ in the experiments are calculated from (17) with $N_u = 114$, $N = 128$, and $D = 1, 2, 3, \cdots, 9$. The maximum $\mathbb{W}$ in the prototype is 321 MHz, which can be achieved by using all available links in the 3×3 MIMO configuration, e.g., $D = 9$. In the performance evaluations, N_{ser} is configured as 1024.

B. Metrics for Performance Evaluation

We store all CFRs into $\mathbb{D}_{\mathsf{train}}$. For Exp. $1, 3, 4, 5, 6$, we construct the testing database $\mathbb{D}_{\mathsf{test}}$ by storing the same CFRs as those in $\mathbb{D}_{\mathsf{train}}$, e.g., $\mathbb{D}_{\mathsf{train}} = \mathbb{D}_{\mathsf{test}}$. Then, using CFRs in $\mathbb{D}_{\mathsf{train}}$ and $\mathbb{D}_{\mathsf{test}}$, we calculate the resonating strength matrix $\mathbb{R}$ with its (i, j)-th entry given by $\gamma[\hat{\mathbb{H}}_i, \hat{\mathbb{H}}_j]$. Here, $\hat{\mathbb{H}}_i$ is the i-th column of $\mathbb{D}_{\mathsf{train}}$ and $\hat{\mathbb{H}}_j$ is the j-th column of $\mathbb{D}_{\mathsf{test}}$. j is denoted as the *testing index*. Notice that the main diagonal entries of $\mathbb{R}$ are 1 since $\gamma[\hat{\mathbb{H}}_i, \hat{\mathbb{H}}_i] \triangleq 1, \forall i$.

Based on $\mathbb{R}$, we evaluate the localization performances by the **true positive rate**, denoted as $\mathbb{P}_{\mathsf{TP}}$, and the **false positive rate**, denoted as $\mathbb{P}_{\mathsf{FP}}$. $\mathbb{P}_{\mathsf{TP}}$ is defined as the probability that the AP localizes the STA to the correct locations, while $\mathbb{P}_{\mathsf{FP}}$ is defined as probability that the AP localizes the STA to the incorrect locations or the null location. For some experiments, we also show the Receiver Operating Characteristic (ROC) curve to highlight the tradeoffs between $\mathbb{P}_{\mathsf{TP}}$ and $\mathbb{P}_{\mathsf{FP}}$ by tuning the threshold Γ.

C. Performance Evaluation

In this part, we demonstrate the performances of the experiments under the optimal Γ settings.

Exp. 1**: LOS and NLOS with** $5cm$ **Resolution**

In Fig. 5, we show the resonating strength matrix $\mathbb{R}$ under different $\mathbb{W}$ in both NLOS and LOS scenarios measured with $5cm$ resolution. As can be seen from Fig. 5, increasing $\mathbb{W}$ reduces the resonating strength among different locations,

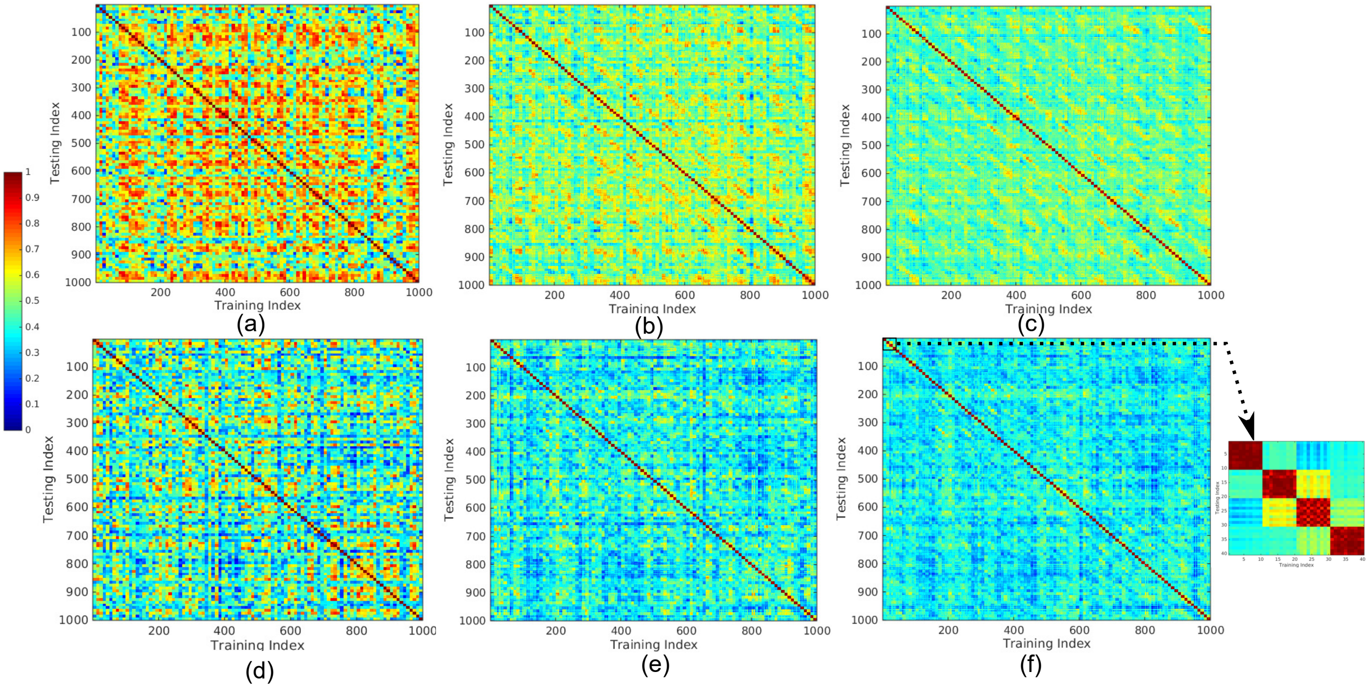

Fig. 5: Results of Exp. 1 under (a) LOS, $\mathbb{W} = 36$ MHz (b) LOS, $\mathbb{W} = 143$ MHz (c) LOS, $\mathbb{W} = 321$ MHz. (d) NLOS, $\mathbb{W} = 36$ MHz (e) NLOS, $\mathbb{W} = 143$ MHz (f) NLOS, $\mathbb{W} = 321$ MHz.

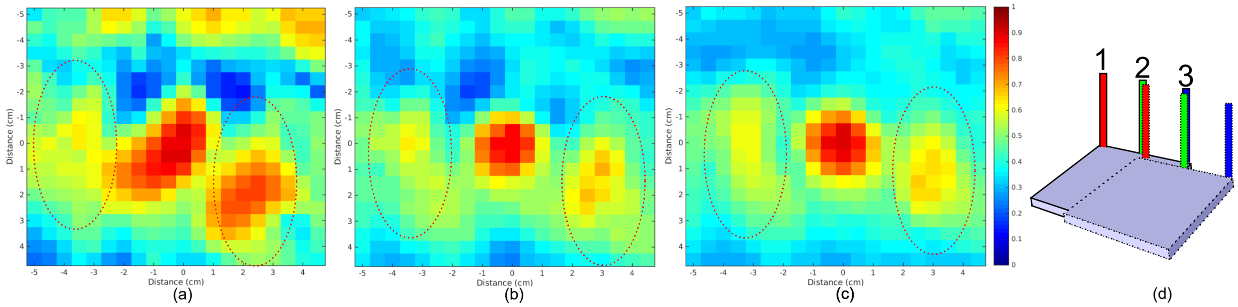

Fig. 6: Results of Exp. 2 under (a) $\mathbb{W} = 36$ MHz (b) $\mathbb{W} = 143$ MHz (c) $\mathbb{W} = 321$ MHz. (d) The antenna coupling effect.

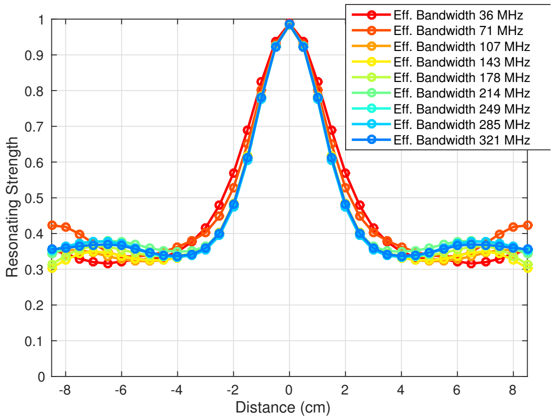

Fig. 7: Decaying of resonating strength with distance.

as can be observed from the decreasing off-diagonal part in $\mathbb{R}$. Therefore, a large $\mathbb{W}$ mitigates the ambiguities among different locations. On the other hand, we illustrate the details of the diagonal part of $\mathbb{R}$ in Fig. 5(f) when $\mathbb{W} = 321$ MHz. The resonating strengths calculated at the same location is close to 1.

In Table I, we elaborate the smallest Γ to achieve $\mathbb{P}_{\mathsf{TP}} \geq 90\%$ with $\mathbb{P}_{\mathsf{FP}} \leq 2\%$. We observe that Γ decreases when $\mathbb{W}$ increases. When $\mathbb{W} = 321$ MHz, the true positive rates reach 100% and 99.93% while the false positive rates are merely 1.80% and 1.56% for the NLOS and LOS scenarios respectively.

The resonating strengths among different locations in the NLOS scenario are lower than those in the LOS scenario, indicating improved location distinctions under NLOS. This is because, in the LOS case, the channel energy is concentrated in the first few multipath components, leading to only a few resolvable multipaths, while in the NLOS case, the channel energy is spread over a large number of multipath components and thus provides richer information of the environment.

Exp. 2: NLOS with $0.5cm$ Resolution

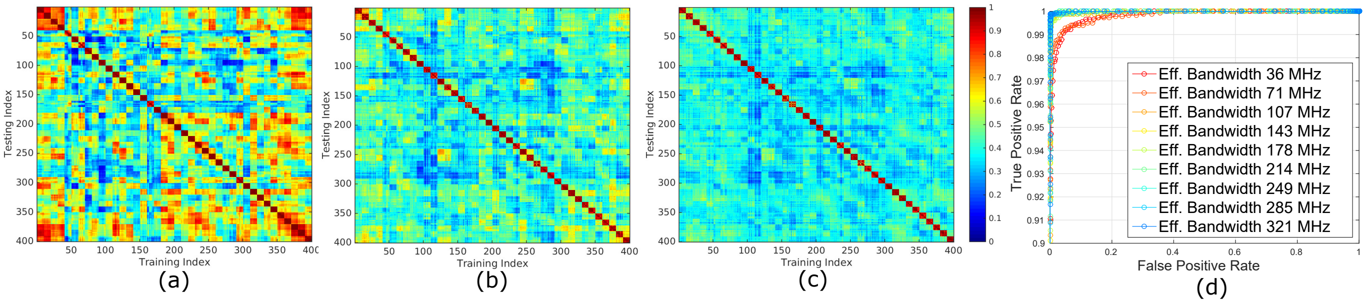

Fig. 8: Results of Exp. 3 under (a) $\mathbb{W} = 36$ MHz (b) $\mathbb{W} = 143$ MHz (c) $\mathbb{W} = 321$ MHz. (d) ROC curve for different $\mathbb{W}$.

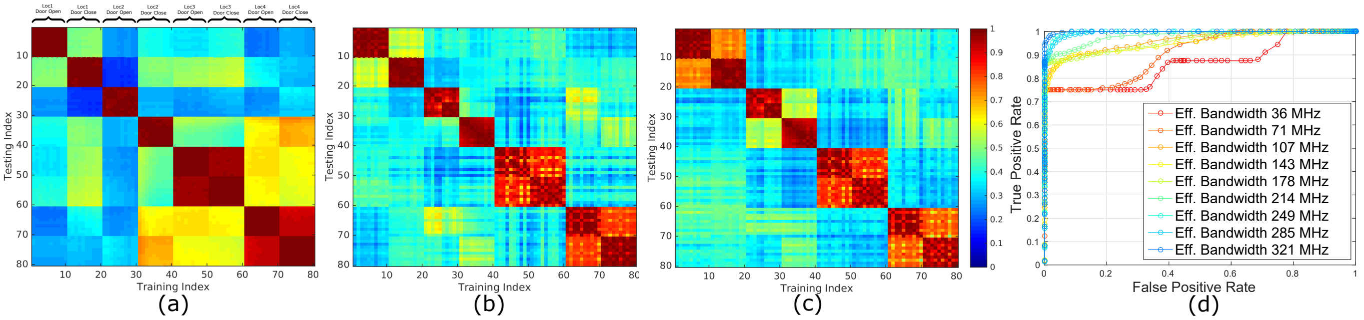

Fig. 9: Results of Exp. 4 under (a) $\mathbb{W} = 36$ MHz (b) $\mathbb{W} = 143$ MHz (c) $\mathbb{W} = 321$ MHz. (d) ROC curve for different $\mathbb{W}$.

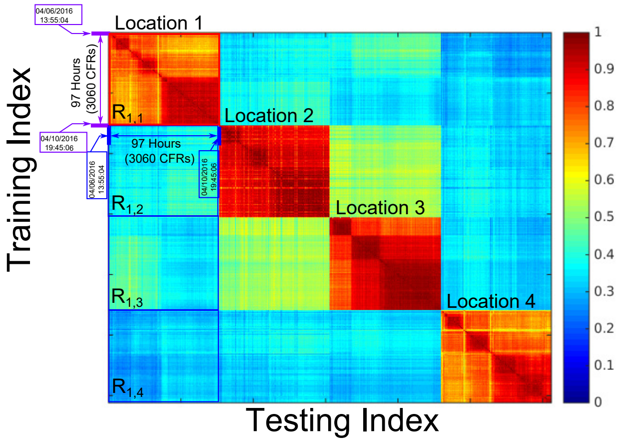

Fig. 10: Results of Exp. 5 in 97 hours of measurements.

We include the CFRs of the 400 locations on the 20×20 testbed into $\mathbb{D}_{\text{train}}$. For $\mathbb{D}_{\text{test}}$, we store the CFRs associated with the middle point on the testbed. The results are shown in Fig. 6(a), (b), (c) with different $\mathbb{W}$. We observe that large resonating strengths are concentrated within a small circular area with a radius of $1 \sim 2cm$ when $\mathbb{W} \geq 143$ MHz, while the resonating strengths are more decentralized when $\mathbb{W} = 36$ MHz. On the other hand, we also observe an area with high resonating strengths in the horizontal direction, marked by the dashed ovals in Fig. 6(a), (b), (c). The reason is justified visually by Fig. 6(d): as we move the STA horizontally in parallel to the antenna positions on the 20×20 grid, the fingerprint obtained at a new location overlaps with one particular fingerprint of a previous location. Due to the antenna coupling effect, the resonating strengths between two horizontally spaced locations can be large.

Ignoring the regions caused by the antenna coupling, and storing CFRs of different positions on the testbed as location-of-interest into $\mathbb{D}_{\text{test}}$, we present the decaying curve of resonating strength when the spatial separation between two locations increases in the unit of $0.5cm$ in Fig. 7. A larger $\mathbb{W}$ accelerates the decaying of the resonating strength and thus provides improved localization accuracy. We conclude that, with appropriate Γ, the proposed IPS can achieve an accuracy of $1 \sim 2cm$.

Exp. 3: Effect of Human Activities
Fig. 8 shows the impact of human activities on the performance of the proposed IPS. Comparing Fig. 8(a), (b), (c), we find that a large $\mathbb{W}$ is important in the presence of environment dynamics. Fig. 8(d) illustrates the ROC curve using different $\mathbb{W}$ which further verifies that a large $\mathbb{W}$ can enhance the localization performance. As shown in Table I, when $\mathbb{W} = 321$ MHz, a threshold of 0.53 suffices to achieve $\mathbb{P}_{\text{TP}} = 99.89\%$ and $\mathbb{P}_{\text{FP}} = 1.74\%$.

Exp. 4: Impact of Door Open/Close
In general, the impact of door opening/closing on localization is more severe than the human activities. In Fig. 9, we illustrate the results using different $\mathbb{W}$. The importance of a large $\mathbb{W}$ is more pronounced in this experiment: according to Table I, when $\mathbb{W} \leq 214$ MHz, we fail to find Γ to satisfy the condition of $\mathbb{P}_{\text{TP}} \geq 90\%, \mathbb{P}_{\text{FP}} \leq 2\%$. The performance improves dramatically with $\mathbb{W} = 321$ MHz, which boosts $\mathbb{P}_{\text{TP}}$ to 98.37% with $\mathbb{P}_{\text{FP}}$ evaluated as 1.70%.

Exp. 5: Localization Performance in 97 Hours

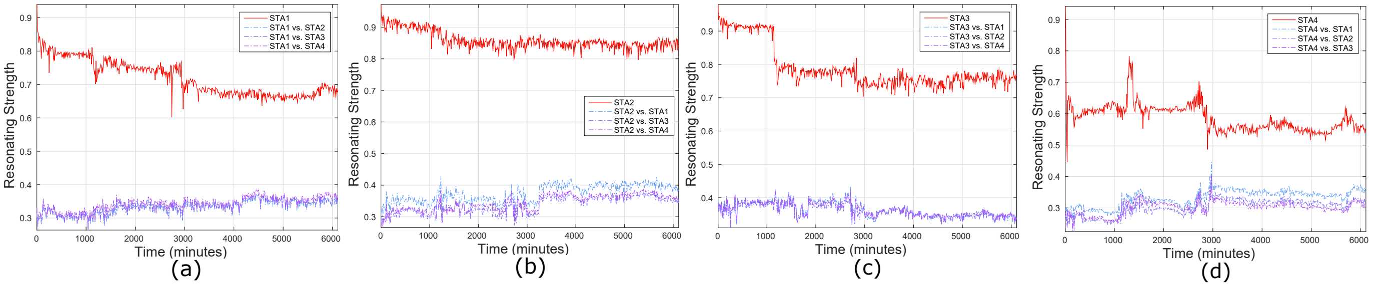

Fig. 11: Time evolution of the average resonating strengths in 97 hours of measurement. (a) STA 1 (b) STA 2 (c) STA 3 (d) STA 4.

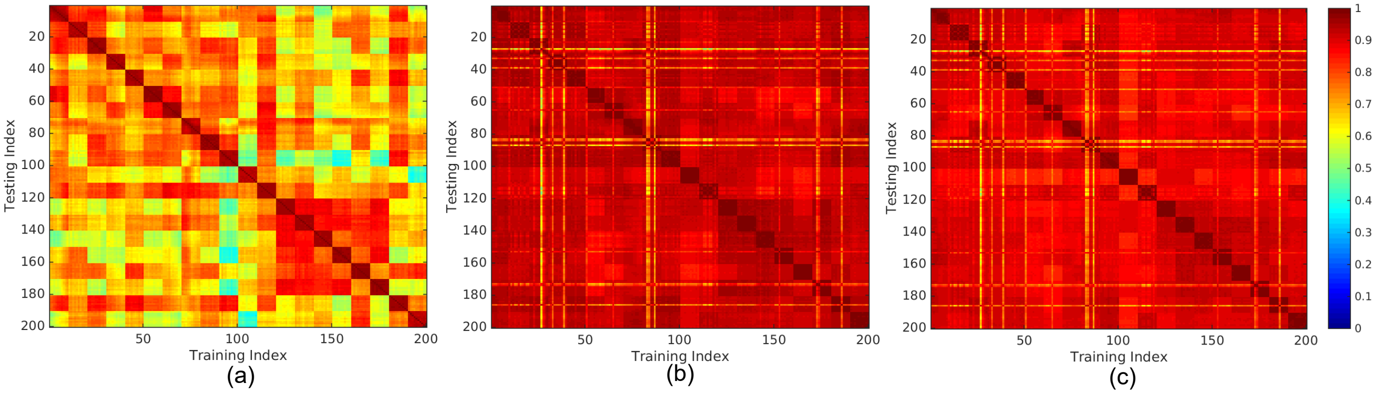

Fig. 12: Results of Exp. 6. (a) $\mathbb{W} = 36$ MHz (b) $\mathbb{W} = 143$ MHz (c) $\mathbb{W} = 321$ MHz.

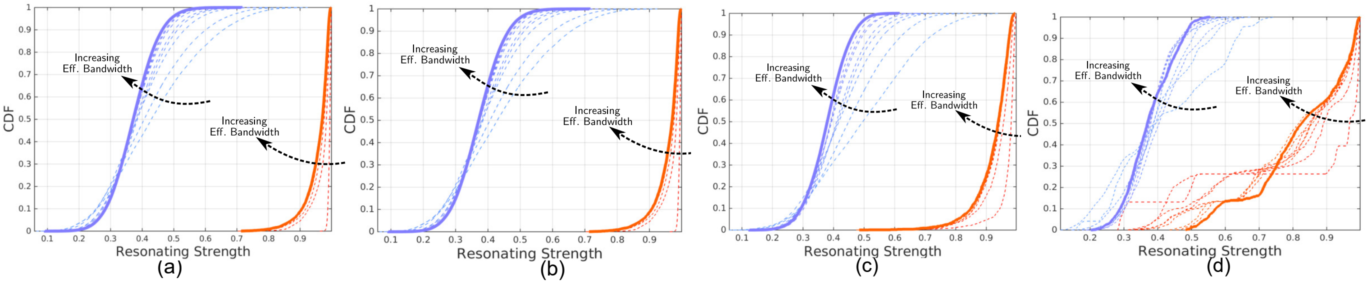

Fig. 13: Impact of $\mathbb{W}$ on the resonating strengths. (a) Exp. 1, LOS (b) Exp. 1, NLOS (c) Exp. 3 (4) Exp. 4.

In Fig. 10, we demonstrate $\mathbb{R}$ for 4 different STAs with positions shown in Fig. 4. $\mathbb{R}$ is computed using $\mathbb{D}_{\text{train}}$ and $\mathbb{D}_{\text{test}}$ composed by all CFRs collected for the 4 STAs. For each STA, we obtain 3060 CFRs over 97 hours. Therefore, the CFRs with training/testing index in the range of $[3060(k-1)+1, 3060k]$ correspond to those CFRs collected by STA k, with $k = 1, 2, 3, 4$.

As an example, we highlight four regions in Fig. 10. $\mathbb{R}_{1,1}$ represents the resonating strengths among CFRs of the same STA 1, and $\mathbb{R}_{1,2}, \mathbb{R}_{1,3}, \mathbb{R}_{1,4}$ denotes the resonating strengths between STA 1 and STA $2, 3, 4$ respectively. Fig. 10 shows that the resonating strengths calculated at the same STA are significantly larger than those calculated among different STA locations, indicating excellent localization performance in the 97 hours of measurement. With $\mathbb{W} = 321$ MHz, we achieve $\mathbb{P}_{\text{TP}} = 99.87\%$ and $\mathbb{P}_{\text{FP}} = 1.65\%$ with $\Gamma = 0.56$.

In Fig. 11, we sketch the time evolution of the resonating strengths at different STA locations in the 97 hours of measurement. For each STA location, we only keep the first CFR obtained at that location into $\mathbb{D}_{\text{train}}$, and store all the other CFRs obtained at different time and at other STA locations into $\mathbb{D}_{\text{test}}$. We observe from Fig. 11 that the resonating strengths decay with time due to CFR variations caused by the environment dynamics, e.g., position change of reflectors such as desks and chairs. Apart from utiziling a fixed $\Gamma = 0.56$ to achieve good localization performance, we can also update $\mathbb{D}_{\text{train}}$ on a regular basis to compensate the performance loss caused by environment dynamics.

Exp. 6: Impact of Power Cycling on Localization Performance

Fig. 12 shows $\mathbb{R}$ with different $\mathbb{W}$ under the experiment setting of Exp. 6. Clearly, when $\mathbb{W} = 36$ MHz, there exists large fluctuation in the resonating strengths and the localization performance can be severely affected. Such fluctuation is significantly suppressed when $\mathbb{W} = 143$ or 321 MHz, which justifies the importance of a large $\mathbb{W}$.

D. Impact of Various Factors

In this part, we investigate the effect of $\mathbb{W}$ on the resonating strengths in several experiments, and then discuss the feasibility of utilizing a predetermined Γ for different experiments.

Impact of Effective Bandwidth on Resonating Strength
In Fig. 13, we illustrate the cumulative density functions (CDFs) of the resonating strengths calculated at the same locations and among different locations under a variety of $\mathbb{W}$ for Exp. 1, 3, and 4. We find that for all experiments, enlarging $\mathbb{W}$ suppresses the resonating strengths calculated for two different locations, while reduces the resonating strengths evaluated at the same locations only gracefully. Therefore, it further validates that it is beneficial to use a large $\mathbb{W}$.

Impact of Using a Universal Γ
For the performance evaluation in Section IV, we assume that the proposed IPS selects a specific Γ to achieve $\mathbb{P}_{\mathsf{TP}} \geq 90\%$ and $\mathbb{P}_{\mathsf{FP}} \leq 2\%$. However, in practice, we might be unable to choose a particular Γ since the environmental dynamics is unpredictable, e.g., random walk of people in the office or opening/closing of the doors, necessitating a universal Γ for the proposed IPS.

We assume that $\Gamma = 0.6$ and $\mathbb{W} = 321$ MHz. The performances are summarized into Table II. As we can see, except Exp. 4, the proposed IPS achieves $\mathbb{P}_{\mathsf{TP}} \geq 99.47\%$ with $\mathbb{P}_{\mathsf{FP}} \leq 3.96\%$. The performance of Exp. 4 with $\Gamma = 0.6$ degrades from the case of $\Gamma = 0.51$ shown in Table I, but still we can achieve $\mathbb{P}_{\mathsf{TP}} = 87.13\%$. One reason for the performance degradation is due to the sensitivity of some particular locations to the object movements. This can be overcome by placing multiple WiFi pairs to enhance the robustness of detection.

	Exp. 1 NLOS	Exp. 1 LOS	Exp. 3 Human Activities	Exp. 4 Door Effect	Exp. 5 Long-term Measurement
$\mathbb{P}_{\mathsf{TP}}(\%)$	100	99.96	99.78	87.13	99.47
$\mathbb{P}_{\mathsf{FP}}(\%)$	0.1392	3.96	0.0038	0	0.0633

TABLE II: Performances with $\Gamma = 0.60$.

V. CONCLUSIONS AND DISCUSSIONS

In this paper, we propose an IPS based on WiFi devices that leverages the TR focusing effect to facilitate centimeter-level accuracy for indoor localization. The proposed IPS fully utilize the spatial diversity in MIMO-OFDM WiFi systems to formulate a large effective bandwidth. Extensive experimental results show that the proposed IPS achieves true positive rates of 99.93% and 100%, and incurs false positive rates of 1.56% and 1.80% under the LOS and NLOS scenarios respectively. Meanwhile, the IPS is robust against the environment dynamics caused by human activities and object movements. Experimental results with a resolution of $0.5cm$ demonstrate an accuracy of $1 \sim 2cm$ achieved by the proposed IPS. To the best of our knowledge, this is the first work that can achieve $1 \sim 2cm$ accuracy for indoor localization by exploiting the spatial diversity on a single-pair of WiFi devices under the NLOS scenarios.

In this work, we assume that the orientations of the three antennas are the same during the training and positioning phase. In practice, the orientations can be different in the two phases, which might negatively affect the performance of the IPS. To overcome this issue, we could either supplement the training database with CFRs of different orientations on each location, or utilize antenna designs that are insensitive to minor antenna rotations. Currently, we are conducting extensive measurements to study the impact of antenna orientations on the performance as well as developing robust methods to counteract this issue.

REFERENCES

[1] T. Gallagher, B. Li, A. Dempster, and C. Rizos, "A sector-based campus-wide indoor positioning system," in *Indoor Positioning and Indoor Navigation (IPIN), 2010 International Conference on*, pp. 1–8, Sept 2010.

[2] K.-L. Sue, "Mambo: A mobile advertisement mechanism based on obscure customer's location by RFID," in *Computing, Measurement, Control and Sensor Network (CMCSN), 2012 International Conference on*, pp. 425–428, July 2012.

[3] L. Wang, W. Liu, N. Jing, and X. Mao, "Simultaneous navigation and pathway mapping with participating sensing," *Wirel. Netw.*, vol. 21, pp. 2727–2745, Nov. 2015.

[4] H. Liu, H. Darabi, P. Banerjee, and J. Liu, "Survey of wireless indoor positioning techniques and systems," *IEEE Trans. Syst., Man, Cybern., Syst.*, vol. 37, pp. 1067–1080, Nov 2007.

[5] J. Hightower, R. Want, and G. Borriello, "SpotON: An indoor 3D location sensing technology based on RF signal strength," UW CSE 00-02-02, University of Washington, Department of Computer Science and Engineering, Seattle, WA, February 2000.

[6] L. Ni, Y. Liu, Y. C. Lau, and A. Patil, "LANDMARC: indoor location sensing using active RFID," in *Pervasive Computing and Communications, 2003. (PerCom 2003). Proceedings of the First IEEE International Conference on*, pp. 407–415, March 2003.

[7] N. Patwari and S. K. Kasera, "Robust location distinction using temporal link signatures," in *Proceedings of the 13th Annual ACM International Conference on Mobile Computing and Networking*, MobiCom '07, (New York, NY, USA), pp. 111–122, ACM, 2007.

[8] J. Zhang, M. H. Firooz, N. Patwari, and S. K. Kasera, "Advancing wireless link signatures for location distinction," in *Proceedings of the 14th ACM international conference on Mobile computing and networking*, MobiCom '08, (New York, NY, USA), pp. 26–37, ACM, 2008.

[9] M. Youssef and A. Agrawala, "The Horus WLAN location determination system," in *Proceedings of the 3rd International Conference on Mobile Systems, Applications, and Services*, MobiSys '05, (New York, NY, USA), pp. 205–218, ACM, 2005.

[10] P. Bahl and V. Padmanabhan, "RADAR: an in-building RF-based user location and tracking system," in *Proc. IEEE INFOCOM*, vol. 2, pp. 775–784 vol.2, 2000.

[11] P. Prasithsangaree, P. Krishnamurthy, and P. Chrysanthis, "On indoor position location with wireless LANs," in *Personal, Indoor and Mobile Radio Communications, 2002. The 13th IEEE International Symposium on*, vol. 2, pp. 720–724 vol.2, Sept 2002.

[12] S. Sen, B. Radunovic, R. R. Choudhury, and T. Minka, "You are facing the Mona Lisa: Spot localization using PHY layer information," in *Proceedings of the 10th International Conference on Mobile Systems, Applications, and Services*, MobiSys '12, (New York, NY, USA), pp. 183–196, ACM, 2012.

[13] J. Xiao, W. K.S., Y. Yi, and L. Ni, “FIFS: Fine-grained indoor fingerprinting system,” in *Computer Communications and Networks (ICCCN), 2012 21st International Conference on*, pp. 1–7, July 2012.

[14] Y. Chapre, A. Ignjatovic, A. Seneviratne, and S. Jha, “CSI-MIMO: Indoor Wi-Fi fingerprinting system,” in *Local Computer Networks (LCN), 2014 IEEE 39th Conference on*, pp. 202–209, Sept 2014.

[15] Z.-H. Wu, Y. Han, Y. Chen, and K. J. R. Liu, “A time-reversal paradigm for indoor positioning system,” *IEEE Trans. Veh. Commun.*, vol. 64, pp. 1331–1339, April 2015.

[16] B. Wang, Y. Wu, F. Han, Y.-H. Yang, and K. J. R. Liu, “Green wireless communications: A time-reversal paradigm,” *IEEE J. Select. Areas Commun.*, vol. 29, pp. 1698–1710, September 2011.

[17] C. Chen, Y. Chen, L. Hung-Quoc, Y. Han, and K. J. R. Liu, “High accuracy indoor localization: A WiFi-based approach,” in *Proc. IEEE International Conference on Acoustics, Speech and Signal Processing (ICASSP)*, March 2016.

[18] B. Bogert, “Demonstration of delay distortion correction by time-reversal techniques,” *Communications Systems, IRE Transactions on*, vol. 5, pp. 2–7, December 1957.

[19] J. Kormylo and V. Jain, “Two-pass recursive digital filter with zero phase shift,” *IEEE Trans. Acoust., Speech, Signal Processing*, vol. 22, pp. 384–387, Oct 1974.

[20] M. Fink, “Acoustic time-reversal mirrors,” in *Imaging of Complex Media with Acoustic and Seismic Waves* (M. Fink, W. Kuperman, J.-P. Montagner, and A. Tourin, eds.), vol. 84 of *Topics in Applied Physics*, Springer Berlin Heidelberg, 2002.

[21] M. Fink, C. Prada, F. Wu, and D. Cassereau, “Self focusing in inhomogeneous media with time reversal acoustic mirrors,” in *Ultrasonics Symposium, 1989. Proceedings., IEEE 1989*, pp. 681–686 vol.2, Oct 1989.

[22] C. Dorme, M. Fink, and C. Prada, “Focusing in transmit-receive mode through inhomogeneous media: The matched filter approach,” in *Ultrasonics Symposium, 1992. Proceedings., IEEE 1992*, pp. 629–634 vol.1, Oct 1992.

[23] F. Han, Y.-H. Yang, B. Wang, Y. Wu, and K. J. R. Liu, “Time-reversal division multiple access over multi-path channels,” *IEEE Trans. Commun.*, vol. 60, pp. 1953–1965, July 2012.

[24] G. Stuber, J. Barry, S. McLaughlin, Y. Li, M. Ingram, and T. Pratt, “Broadband MIMO-OFDM wireless communications,” *Proceedings of the IEEE*, vol. 92, pp. 271–294, Feb 2004.

[25] M. Speth, S. Fechtel, G. Fock, and H. Meyr, “Optimum receiver design for wireless broad-band systems using OFDM—Part I,” *IEEE Trans. Commun.*, vol. 47, pp. 1668–1677, Nov 1999.